

Complete-Q Model for Poro-Viscoelastic Media in Subsurface Sensing: Large-Scale Simulation With an Adaptive DG Algorithm

Qiwei Zhan¹, *Student Member, IEEE*, Mingwei Zhuang, Zhennan Zhou, Jian-Guo Liu,
and Qing Huo Liu², *Fellow, IEEE*

Abstract—In this paper, full mechanisms of dissipation and dispersion in poro-viscoelastic media are accurately simulated in time domain. Specifically, four Q values are first proposed to depict a poro-viscoelastic medium: two for the attenuation of the bulk and shear moduli in the solid skeleton, one for the bulk modulus in the pore fluid, and the other one for the solid-fluid coupling. By introducing several sets of auxiliary ordinary differential equations, the Q factors are efficiently incorporated in a high-order discontinuous Galerkin algorithm. Consequently, in the mathematical sense, the Riemann problem is exactly solved, with the same form as the inviscid poroelastic material counterpart; in the practical sense, our algorithm requires nearly negligible extra time cost, while keeping the governing equations almost unchanged. Parenthetically, an arbitrarily nonconformal-mesh technique, in terms of both h- and p-adaptivity, is implemented to realize the domain decomposition for a flexible algorithm. Furthermore, our algorithm is verified with an analytical solution for the half-space modeling. A validation with an independent numerical solver, and an application to a large-scale realistic complex topography modeling demonstrate the accuracy, efficiency, flexibility, and capability in realistic subsurface sensing.

Index Terms—Discontinuous Galerkin, domain decomposition, porous viscoelasticity, Q-factor, subsurface sensing.

I. INTRODUCTION

IN THE realm of geoscience subsurface sensing, the Biot's biphasic model is pervasively used for a more accurate description of realistic materials [1]–[3]. However, purely poroelastic model may not be sufficient. Carcione [4, p. 280] elucidates the importance of incorporating viscosity effects into the poroelastic media, by comparing the recorded seismograms and synthetic waveforms.

Manuscript received July 25, 2018; revised November 8, 2018; accepted January 1, 2019. Date of publication February 11, 2019; date of current version June 24, 2019. The work of Q. Zhan was supported by the JOHN T. CHAMBERS Scholar Award fund at Duke University, Durham, NC 27708 USA. (*Corresponding author: Qing Huo Liu.*)

Q. Zhan and Q. H. Liu are with the Department of Electrical and Computer Engineering, Duke University, Durham, NC 27708 USA (e-mail: qhliu@duke.edu).

M. Zhuang is with the Institute of Electromagnetics and Acoustics, Xiamen University, Xiamen 361005, China.

Z. Zhou is with the Beijing International Center for Mathematical Research, Peking University, Beijing 100871, China.

J.-G. Liu is with the Department of Physics and Mathematics, Duke University, Durham, NC 27708 USA.

Color versions of one or more of the figures in this paper are available online at <http://ieeexplore.ieee.org>.

Digital Object Identifier 10.1109/TGRS.2019.2891691

Physically speaking, the dispersion and dissipation effects of poroelastic waves, originate from not only the viscous solid skeleton but also the infilling fluid and their interaction. Mathematically speaking, the governing equations for poroelastic waves are comprised of: 1) dynamic Biot's motion equation, with respect to divergence of stresses in the viscous skeleton (also called as lattice, matrix, or frame) and 2) dynamic Darcy's law, with respect to the gradient of pressure in the viscous pore fluid. In this paper, we will propose a complete-Q model, which is described by the stress-strain constitutive relationship [4, p. 276].

However, numerical implementation of poro-viscoelastic waves remains a delicate task for current numerical solvers. Heuristically, the viscosity in poroelastic media can be incorporated, in analogy with the existing viscoelastic modeling. Typically, two approaches have been utilized to resolve the viscosity-induced memory effects: the spatial/temporal fractional-derivative operator and the auxiliary variable approximation. The former is not affordable for 3-D large-scale engineering problems, since it involves convolutional integrals and requires tremendous storages of the entire-history variables; nevertheless, the truncation principle is a possibility for strong attenuation, especially for small Q values [5]–[7]. Therefore, it is preferable to evaluate the time-domain stress-strain relation efficiently, by resorting to the auxiliary differential equations [8, Ch. 3]. Likewise, in electromagnetic dispersive media, the auxiliary differential equation method has widely been used [9].

In viscoelastic modeling, by introducing several sets of auxiliary differential equations, the generalized Zener body (GZB) and the generalized Maxwell body (GMB) are two prevailing rheological solutions. They are comprised of either serial or parallel combinations of Newton liquids and Hook springs. Conventionally, the GMB model is widely adopted in velocity-stress-based finite-difference time-domain (FDTD) algorithm [8]. However, in the velocity-stress-based discontinuous Galerkin (DG) framework for viscoelastic modeling, the exact Riemann solution is usually intractable [10]–[12]. Specifically, the auxiliary equations are still partial differential equations, thus involving spatially nonlocal evaluation.

In this paper, we aim to efficiently evaluate the complete-Q model in time domain: the GMB is used in the DG algorithm,

based on velocity–strain variables. The new contributions we deliver in this paper are given in the following.

- 1) A complete-Q model, with four Q values corresponding to the physical insight, is proposed to fully incorporate dispersions and dissipations of an isotropic porous medium for the first time.
- 2) We leverage several sets of auxiliary ordinary differential equations (ODEs), thus only involving both temporally and spatially localized damping, to accurately capturing viscosity effects.
- 3) Consequently, from the perspective of mathematics, the Riemann problem is exactly solved, with the same form as the inviscid poroelastic material counterpart; from the perspective of practicality, our algorithm requires nearly negligible extra time cost, while keeping the governing equations almost unchanged.

This paper is organized as follows. Section II provides the governing equations for poroelastic media in the low-frequency regime. Section III provides a complete-Q model, and modifies the stress–strain constitutive relationship by adding extra anelastic functions, which are governed by the ODEs in lieu of the convolutional integral. Section IV applies a nonconformal DG algorithm to the hyperbolic system. An exact Riemann solution is obtained in Section V. Section VI shows numerical validations and verifications. Conclusions are drawn in Section VII.

II. GOVERNING EQUATIONS IN THE LOW-FREQUENCY REGIME

For general poroelastic media, the Biot’s dynamic equation and Darcy’s law read, respectively [4, p. 254],

$$\frac{\partial \tau_{ij}}{\partial x_j} = \rho \frac{\partial v_i}{\partial t} + \rho_f \frac{\partial w_i^f}{\partial t} + F_i^1 \quad (1a)$$

$$-\frac{\partial p}{\partial x_i} = \rho_f \frac{\partial v_i}{\partial t} + \Psi * \frac{\partial w_i^f}{\partial t} + F_i^2 \quad (1b)$$

where x_j ($j = 1$ to 3) and t are the independent variables, corresponding to the Cartesian spatial coordinate and time axis, respectively, and v_i and w_i^f are the dependent variables, corresponding to the particle velocity of the solid frame and the pore-fluid particle velocity dispersion (i.e., the velocity relative to the solid frame), respectively. Note that τ_{ij} ($i, j = 1$ to 3) and p are the stress tensor and the pore-fluid pressure, respectively, which can be calculated from the dependent variables via the constitutive relation in Section III. In addition, we have constants’ definitions: ρ is the density of the poroelastic medium as $\rho = (1 - \phi)\rho_s + \phi\rho_f$, ϕ is the porosity of the poroelastic medium, ρ_s is the density of the solid frame, and ρ_f is the density of the fluid. In addition, F_i^1 and F_i^2 correspond to body force densities imposed on the solid frame and the pore fluid, respectively. Note that “*” implies a time convolutional integral. Especially, $\Psi(t)$ is the viscodynamic operator

$$\Psi(t) = \rho^w \delta(t) + \frac{\nu}{\kappa} \chi(t) H(t) \quad (2)$$

where $\delta(t)$ is the Dirac delta function, $H(t)$ is the Heaviside function, ρ^w is the fluid inertia: $\rho^w = \rho_f T / \phi$, ν is the fluid

viscosity, κ is the permeability of the solid matrix, and T is tortuosity of the solid matrix. Note that $f_{cr} = (\nu/\kappa)/\rho^w$ is the Biot’s critical frequency [13]. For the low-frequency regime ($f < f_{cr}$), the fluid is with a Poiseuille-type behavior: $\chi(t) = 1$. For the convenience of solving problems in time domain, (1) is further derived by Cramer’s rule, leading to

$$\rho^{(1)} \frac{\partial v_i}{\partial t} = \frac{\partial \tau_{ij}}{\partial x_j} + \beta^{(1)} \frac{\partial p}{\partial x_i} + \beta^{(1)} \frac{\nu}{\kappa} w_i^f + F_i^{(1)} \quad (3a)$$

$$\rho^{(2)} \frac{\partial w_i^f}{\partial t} = -\frac{\partial \tau_{ij}}{\partial x_j} - \beta^{(2)} \frac{\partial p}{\partial x_i} - \beta^{(2)} \frac{\nu}{\kappa} w_i^f + F_i^{(2)} \quad (3b)$$

with

$$\begin{aligned} \rho^{(1)} &= \rho - \frac{\rho_f^2}{\rho^w} & \rho^{(2)} &= \frac{\rho}{\rho_f} \rho^w - \rho_f \\ \beta^{(1)} &= \frac{\rho_f}{\rho^w} & \beta^{(2)} &= \frac{\rho}{\rho_f} \\ F_i^{(1)} &= -F_i^1 + \beta^{(1)} F_i^2 & F_i^{(2)} &= F_i^1 - \beta^{(2)} F_i^2 \end{aligned} \quad (4)$$

Note this system will be closed by the constitutive relation provided in Section III.

III. GMB-BASED CONSTITUTIVE RELATION

A. Lossless Poroelastic Medium

For a porous medium with pure elasticity, the constitutive relationship in a matrix form, subject to Voigt notation [8, p. 42], reads

$$\boldsymbol{\tau} = \mathbf{D} \boldsymbol{\epsilon} \quad (5)$$

where

$$\boldsymbol{\tau}_{7 \times 1} = (\tau_{xx}, \tau_{yy}, \tau_{zz}, \tau_{yz}, \tau_{xz}, \tau_{xy}, -p)^\top \quad (6)$$

is comprised of the total stresses (rather than the effective stresses for the frame) and fluid pressure for the pore, and

$$\boldsymbol{\epsilon}_{7 \times 1} = (\epsilon_{xx}, \epsilon_{yy}, \epsilon_{zz}, \gamma_{yz}, \gamma_{xz}, \gamma_{xy}, -\zeta)^\top \quad (7)$$

is comprised of matrix strains and fluid strain (i.e., the variation of the fluid content). The detailed expressions for the solid matrix strain are

$$\begin{aligned} \epsilon_{ij} &:= \frac{\partial u_i}{\partial x_j}, \quad \text{for } i = j \\ \gamma_{ij} &:= \frac{\partial u_i}{\partial x_j} + \frac{\partial u_j}{\partial x_i}, \quad \text{for } i \neq j \end{aligned} \quad (8)$$

where u_i is the displacement: $\partial u_i / \partial t := v_i$, and the formulation of the fluid-infilling pore strain rate is

$$-\frac{\partial \zeta}{\partial t} := \partial_i \cdot w_i^f. \quad (9)$$

The detailed expression for \mathbf{D} reads

$$\mathbf{D}_{7 \times 7} = \begin{pmatrix} M_P & 0 & 0 & 0 & 0 & 0 & M\alpha \\ & M_P & 0 & 0 & 0 & 0 & M\alpha \\ 0 & 0 & M_P & 0 & 0 & 0 & M\alpha \\ 0 & 0 & 0 & \mu^m & 0 & 0 & 0 \\ 0 & 0 & 0 & 0 & \mu^m & 0 & 0 \\ 0 & 0 & 0 & 0 & 0 & \mu^m & 0 \\ -\bar{M}\alpha & -\bar{M}\alpha & -\bar{M}\alpha & -\bar{0} & -\bar{0} & -\bar{0} & -\bar{M} \end{pmatrix} \quad (10)$$

with

$$\begin{aligned} M_P &= \bar{K} + \frac{4}{3}\mu^m + M\alpha^2 \\ \alpha &= 1 - \frac{\bar{K}}{K_s} \end{aligned} \quad (11)$$

where \bar{K} is the frame bulk modulus, μ^m is the frame shear modulus, and α is the generalized effective stress component. Note that M is the fluid-solid coupling modulus, with the expression

$$M = \frac{K_s}{(1 - \bar{K}/K_s) - \phi(1 - K_s/K_f)} \quad (12)$$

where K_s is the material's bulk modulus, K_f is the fluid bulk modulus, and ϕ is the matrix porosity.

B. Poro-Viscoelastic Medium

For a GMB-based poro-viscoelastic medium with N relaxation mechanisms, the stress $\boldsymbol{\tau}$ not only depends on strain $\boldsymbol{\epsilon}$ (just like the purely elastic media) but also the anelastic functions $\{\boldsymbol{\theta}^{(n)}\}$. We write this relationship as [8, p. 43]

$$\boldsymbol{\tau} = \mathbf{D}^U \boldsymbol{\epsilon} - \sum_{n=1}^N \mathcal{D}^{(n)} \boldsymbol{\theta}^{(n)} \quad (13)$$

where

$$\boldsymbol{\theta}^{(n)} = (\theta_{xx}^{(n)}, \theta_{yy}^{(n)}, \theta_{zz}^{(n)}, 2\theta_{yz}^{(n)}, 2\theta_{xz}^{(n)}, 2\theta_{xy}^{(n)}, \theta_p^{(n)})^\top \quad (14)$$

is controlled by the ODE as

$$\frac{\partial}{\partial t} \boldsymbol{\theta}^{(n)} + \omega_n \boldsymbol{\theta}^{(n)} = \omega_n \boldsymbol{\epsilon} \quad (15)$$

where ω_n is the relaxation angular frequency [14, eq. 6]. It is worth noting that the unrelaxed moduli \mathbf{D}^U is usually not the same as the regular reference moduli \mathbf{D} measured at the reference angular frequency ω_r . Furthermore, it is also worth noting that the *attenuation moduli* $\mathcal{D}^{(n)}$ is nothing different from the unrelaxed moduli \mathbf{D}^U , but a linear mapping relationship for every corresponding entry [8, p. 44]

$$\mathcal{D}_{ij}^{(n)} = Y_{ij}^{(n)} \mathbf{D}_{ij}^U \quad (16)$$

where no summation convention is applied and $\{Y_{ij}^{(n)}\}$ is called as the anelastic ratio matrix. Note that unrelaxed modulus is calculated as

$$\mathcal{M}^U = \mathcal{M}_r \frac{R + \Theta_1}{2R^2} \quad (17)$$

with

$$\begin{aligned} R &= \sqrt{\Theta_1^2 + \Theta_2^2} \\ \Theta_1 &= 1 - \sum_{n=1}^N Y_{ij}^{(n)} \frac{\omega_n^2}{\omega_n^2 + \omega_r^2} \\ \Theta_2 &= \sum_{n=1}^N Y_{ij}^{(n)} \frac{\omega_n \omega_r}{\omega_n^2 + \omega_r^2}. \end{aligned} \quad (18)$$

C. Complete-Q Model and the Q Transformation Rule

From Section III-B, we can observe that the paramount step to construct the new constitutive relation is the determination of the anelastic ratio matrix $\{Y_{ij}^{(n)}\}$. Therefore, this section focuses on this issue.

In retrospect, (10) suggests that in addition to the two elastic properties of the frame, \bar{K} and μ^m , another two input parameters, such as M and α , are required for the constitutive relation of a purely elastic porous medium. Intuitively, a complete-Q model requires four attenuation parameters to depict a poro-viscoelastic medium: $Q_{\bar{K}}$ and Q_{μ^m} for the attenuation of the bulk and shear moduli in the solid skeleton, respectively, Q_{K_f} for the bulk modulus in the pore fluid, and Q_{K_s} implicitly for the solid-fluid coupling. However, it is still not suitable for a direct extension of (10) from purely elastic to the viscoelastic scenario; nevertheless, with this physical insight, it is, therefore, meaningful to explore the Q value transformation rule below.

Kjartansson [15] provides quality factor definition, based on the Caputo fractional derivative. In time domain, the modulus \mathcal{M} , any entry in D_{IJ} ($I, J = 1$ to 7), involves a Caputo fractional derivative operator ${}_0^C D_t^{2\gamma} := \partial^{2\gamma} / \partial t^{2\gamma}$ as

$$\mathcal{M}(t) = \left(\frac{\mathcal{M}_0}{\omega_r^{2\gamma}} \right) {}_0^C D_t^{2\gamma} \quad (19)$$

with

$$\mathcal{M}_0 = \mathcal{M}_r \cos^2 \left(\frac{\pi\gamma}{2} \right) \quad (20)$$

and constant fractional order

$$\gamma = \frac{1}{\pi} \arctan \frac{1}{Q} \quad (21)$$

where \mathcal{M}_r is the reference modulus. In frequency domain, \mathcal{M} becomes a much simpler complex value with a fractional exponent as

$$\mathcal{M}(\omega) = \mathcal{M}_0 \left(\frac{i\omega}{\omega_r} \right)^{2\gamma}. \quad (22)$$

It is worth noting that with this expression, the analytical solutions can be extended from purely poroelastic media to viscous poroelastic media by complexifying the moduli [16]. Combining (21) and (22), we get an alternative definition of the quality factor, in terms of the tangential loss as

$$Q = \frac{\Re(\mathcal{M})}{\Im(\mathcal{M})} \quad (23)$$

where the identity

$$i^{2\gamma} = (e^{i\pi/2})^{2\gamma} = \cos(\pi\gamma) + i \sin(\pi\gamma) \quad (24)$$

has been used.

Now it is ready to propose a Q value transformation rule as the following.

- 1) Given that complete-Q parameters $\{Q_{\bar{K}}, Q_{\mu^m}, Q_{K_f}, Q_{K_s}\}$ are known, we can get the corresponding complex moduli $\{\tilde{\bar{K}}, \tilde{\mu}^m, \tilde{K}_f, \tilde{K}_s\}$, according to (22). Then, substituting them into (11) and (12), we can get the corresponding complex moduli $\{\tilde{\alpha}, \tilde{M}\}$.

- 2) Substituting all these complex moduli into (10), we can construct a complex elasticity matrix $\tilde{\mathbf{D}}$.
- 3) Now for every nonzero entry \tilde{D}_{IJ} , according to the new quality definition (23), we can obtain a quality factor Q_{IJ} , which may be frequency dependent.
- 4) According to the correspondence principle, for every nonzero entry Q_{IJ} , we can perform the Q-factor fitting to obtain the anelastic ratios $\{Y_{ij}^{(n)}\}$ [14, eq. 6], [17].

IV. DG FORMULATION

A. Conservation Law System for the Poro-Viscoelastic Equation

Combining (3), (8), (9), and (15), we can compactly arrive at a conservation form, by omitting the excitations and lossy terms

$$\frac{\partial \mathbf{q}}{\partial t} = \frac{\partial \mathbf{f}}{\partial x} + \frac{\partial \mathbf{g}}{\partial y} + \frac{\partial \mathbf{h}}{\partial z} \quad (25)$$

where \mathbf{q} , \mathbf{f} , \mathbf{g} , and \mathbf{h} are with the dimension of $(13 + 7N) \times 1$

$$\begin{aligned} \mathbf{q} &= \left(\rho^{(1)}v_x, \rho^{(1)}v_y, \rho^{(1)}v_z, \rho^{(2)}w_x^f, \rho^{(2)}w_y^f, \rho^{(2)}w_z^f, \right. \\ &\quad \left. \epsilon_{xx}, \epsilon_{yy}, \epsilon_{zz}, \gamma_{yz}, \gamma_{xz}, \gamma_{xy}, -\zeta, \right. \\ &\quad \left. \theta_{xx}^{(n)}, \theta_{yy}^{(n)}, \theta_{zz}^{(n)}, 2\theta_{yz}^{(n)}, 2\theta_{xz}^{(n)}, 2\theta_{xy}^{(n)}, \theta_p^{(n)}, \dots \right)^\top \\ \mathbf{f} &= \left(\tau_{xx} + \beta^{(1)}p, \tau_{xy}, \tau_{xz}, -\tau_{xx} - \beta^{(2)}p, -\tau_{xy}, -\tau_{xz}, \right. \\ &\quad \left. v_x, 0, 0, 0, v_z, v_y, w_x^f, \right. \\ &\quad \left. \mathbf{0}_{1 \times 7N} \right)^\top \\ \mathbf{g} &= \left(\tau_{xy}, \tau_{yy} + \beta^{(1)}p, \tau_{yz}, -\tau_{xy}, -\tau_{yy} - \beta^{(2)}p, -\tau_{yz}, \right. \\ &\quad \left. 0, v_y, 0, v_z, 0, v_x, w_y^f, \right. \\ &\quad \left. \mathbf{0}_{1 \times 7N} \right)^\top \\ \mathbf{h} &= \left(\tau_{xz}, \tau_{yz}, \tau_{zz} + \beta^{(1)}p, -\tau_{xz}, -\tau_{yz}, -\tau_{zz} - \beta^{(2)}p, \right. \\ &\quad \left. 0, 0, v_z, v_y, v_x, 0, w_z^f, \right. \\ &\quad \left. \mathbf{0}_{1 \times 7N} \right)^\top. \end{aligned} \quad (26)$$

This system is closed by the constitutive relationship (13). Furthermore, this equation is a hyperbolic system, which will be demonstrated in Section V.

B. DG Discretization

In contrast to the conventional finite-element method, every element is treated as one integral domain Ω in the discontinuous Galerkin Method. Arbitrary high-order nodal basis functions can be used, by weakly imposing the continuity boundary conditions across the interface $\partial\Omega^n := \Gamma$, via a numerical flux. Testing (25) by the function W , and integrating it over Ω , then taking the integral by parts provide [18], [19]

$$\begin{aligned} \int_{\Omega} W \frac{\partial \mathbf{q}}{\partial t} d\Omega &= \int_{\Omega} W \nabla \cdot (\mathbf{f} \hat{x} + \mathbf{g} \hat{y} + \mathbf{h} \hat{z}) d\Omega \\ &= \oint_{\partial\Omega^n} \mathbf{T}^{-1} W \tilde{\mathbf{h}}^* d\Gamma \\ &\quad - \int_{\Omega} \left(\frac{\partial W}{\partial x} \mathbf{f} + \frac{\partial W}{\partial y} \mathbf{g} + \frac{\partial W}{\partial z} \mathbf{h} \right) d\Omega \end{aligned} \quad (27)$$

where we evaluate integral on the surface, whose normal unit is parallel with \tilde{z} in the local coordinates, by a rotation matrix

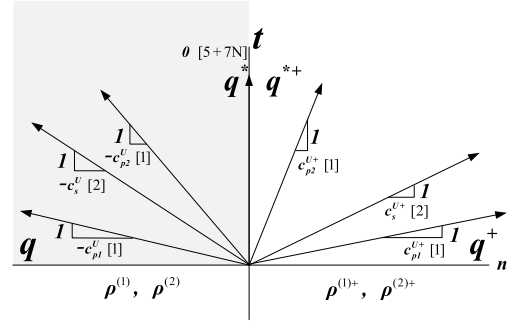


Fig. 1. Characteristic lines: distinct wave propagation speeds and directions are shown along the normal direction. The numbers of each wave speed are provided in the brackets along each line.

\mathbf{T} [4, p. 9]; accordingly, the flux variables are denoted by a tilde notation. Note that an asterisk notation implies that an exact Riemann solution is applied, which is an essential feature of the DG algorithm [20].

C. hp-Adaptivity Version of the DG Algorithm

Modern numerical methods should be amenable to the adaptivity and efficiency in large multiscale engineering/industry problems [21]–[23]. In this paper, we apply the arbitrarily nonconformal technique to realize a kind of hp-adaptivity version DG algorithm [24]. Recently, we have successfully implemented it for the simulation of 3-D elastic waves in an arbitrary high-order DG framework [14], [18], [19], [25], [26]. Compared with the multigrid version nonconformal technique, this new technique provides much more flexibility, since the element types are totally independent between two adjacent regions.

V. UPWIND FLUX FOR ODE-BASED VISCOUS POROELASTIC WAVES

Thanks to the surface integral in the locally rotated coordinates in (27), we can simply solve 1-D Riemann problem as

$$\frac{\partial \mathbf{q}}{\partial t} - \frac{\partial \mathbf{h}}{\partial z} = 0. \quad (28)$$

Note that for brevity, we have removed the tilde notation above, but this Riemann problem is actually solved in the local coordinates. We can obtain the Jacobian matrix as [27, p. 88]

$$[C_{ij}] = \frac{\partial h_i}{\partial q_j}. \quad (29)$$

Note that the entries in (29) from 14 to $13 + 7N$, totally $7N$, are exactly null. Therefore, this proposed velocity–strain-based formulation only adds $7N$ more nonpropagating eigenvalues: this is mathematical perspective for local damping, instead of nonlocal attenuation. This locality is valid in both temporal and spatial sense, thus leading to an efficient evaluation of viscoelasticity. This fact is more clearly shown as the characteristic line in Fig. 1, also indicating the hyperbolicity of the poroelastic wave system equation [27, p. 45].

In this ODE-based framework, the exact Riemann problem can be exactly solved, with an exactly same form as the

TABLE I
POROELASTIC PARAMETERS FOR THE HALF-SPACE MODELING

K_s (GPa)	\bar{K} (GPa)	μ (GPa)	K_f (GPa)	ρ_s (kg/m ³)
80	7	8	5.25	3200
ρ_f (kg/m ³)	ϕ	T	ν/κ (Pa·s/D)	
1000	0.2	2.5	0	

equations without auxiliary ODEs; whereas it is intractable to obtain a Riemann solver for those partial differential equation (PDE)-based methods [10]. Following the same procedures in [28] and [14], we can obtain the exact Riemann solution for the poro-viscoelastic waves

$$\begin{aligned} \mathbf{H}^* - \mathbf{H} &= \begin{pmatrix} \mathbf{Z}^U (\mathbf{Z}^U + \mathbf{Z}^{U+})^{-1} & \mathbf{Z}^U (\mathbf{Z}^U + \mathbf{Z}^{U+})^{-1} \mathbf{Z}^{U+} \\ (\mathbf{Z}^U + \mathbf{Z}^{U+})^{-1} & (\mathbf{Z}^U + \mathbf{Z}^{U+})^{-1} \mathbf{Z}^{U+} \end{pmatrix} \\ &\quad \times (\mathbf{H}^+ - \mathbf{H}) \end{aligned} \quad (30)$$

where the superscript “+” means a variable from the opposite side of the interface. Note that \mathbf{Z}^U is the unrelaxed generalized wave impedance matrix with the size of 4×4 [25], [28], \mathbf{H} is the stress(pressure)-velocity vector

$$\mathbf{H} = \left(\tau_{xz} \quad \tau_{yz} \quad \tau_{zz} \quad p; \quad v_z \quad v_y \quad v_x \quad w_z^f \right)^T. \quad (31)$$

VI. NUMERICAL IMPLEMENTATION

A. Half-Space Modeling With Variant Q Factors

This example aims to validate the accuracy and efficiency of the proposed high-order DG algorithm, applied to the isotropic half-space modeling, where the medium is with viscous poroelastic material with variant Q factors. Table I gives the poroelastic parameters. The physical domain is $[-250, 250] \times [-250, 250] \times [-500, 0]$ m³, which is discretized by $17 \times 17 \times 17$ hexahedral elements in X/Y/Z directions, correspondingly. A perfectly matched layer, with the thickness of one-element, is attached to each surrounding side at planes $X = -250, 250$ m, $Y = -250, 250$ m, and $Z = -500$ m, except the top free boundary $Z = 0$ m, to absorb outgoing waves [29], [30]. The excitation is a z-polarized source, added in (1a), which has a Ricker wavelet source time function with the peak frequency $f_c = 50$ Hz. The source and receiver are located at $(0, 0, -300)$ m and $(200, 0, -450)$ m, respectively. The nodal basis function over a hexahedron is with the order of 12 [18, eq. 6], thus leading to 2.17 points per wavelength, corresponding to the maximum frequency ($3.5f_c$). Three relaxation mechanisms are used, and the reference frequency is chosen as $f_r = 10$ Hz [14, Fig. 2 and Table 1]. We extend the analytical solutions from purely poroelastic media to viscous poroelastic media by complexifying the moduli. Fig. 2 shows the waveform comparisons of the v_z components for different Q factors, obtaining a good agreement between our algorithm and the analytical solution [16], even after many-wavelength propagation. This corroborates the high accuracy and efficiency of the high-order method [31]. Furthermore, we can observe that the waveform

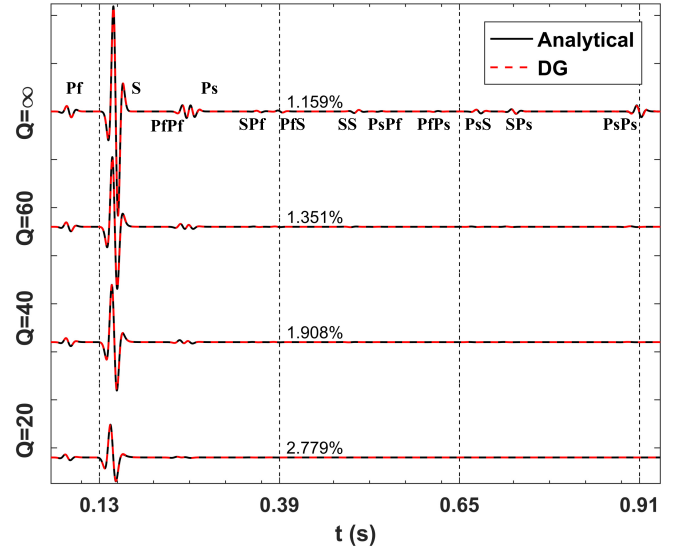


Fig. 2. Comparisons of v_z waveforms between the analytical solution and the DG algorithm, for different quality factors ($Q = Q_P = Q_S = Q_{K_S} = Q_{K_f}$). The waveforms are normalized to the one from lossless media. The relative root-mean-square differences are marked along each waveform, and the twelve seismic phases are marked.

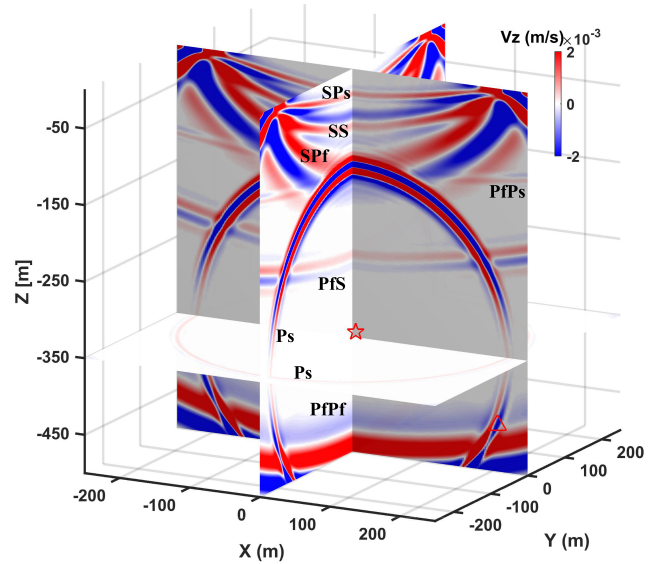


Fig. 3. Snapshot of v_z fields at $t = 0.26$ s. The isotropic poroelastic medium is with the quality factor $Q = Q_P = Q_S = Q_{K_S} = Q_{K_f} = 60$. The source and receiver are marked as a star and a triangle, respectively. The seismic phases are also marked along each wavefront.

is slightly left shifted, whereas the amplitude is increasingly attenuated, when Q decreases. Fig. 3 provides the snapshot of the z-component solid particle velocity for the solid skeleton: we can clearly observe the direct wave (i.e., slow P wave Ps), and three-type wave splitting due to the reflection of the top free boundary, from the direct fast P wave (i.e., PpPf, PpS, and PpPs), and from the direct S wave (i.e., SPf, SS, and SPs).

B. Multilayer Modeling With the hp -Adaptivity Technique

This example shows a multilayer model as shown in Fig. 4, with high-contrast realistic material properties provided

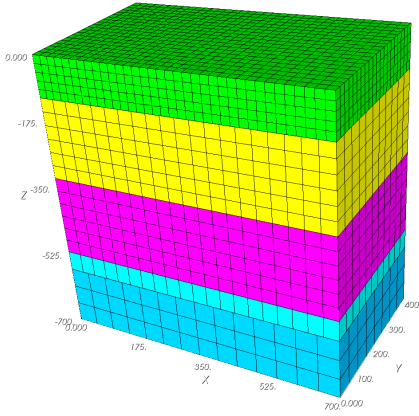


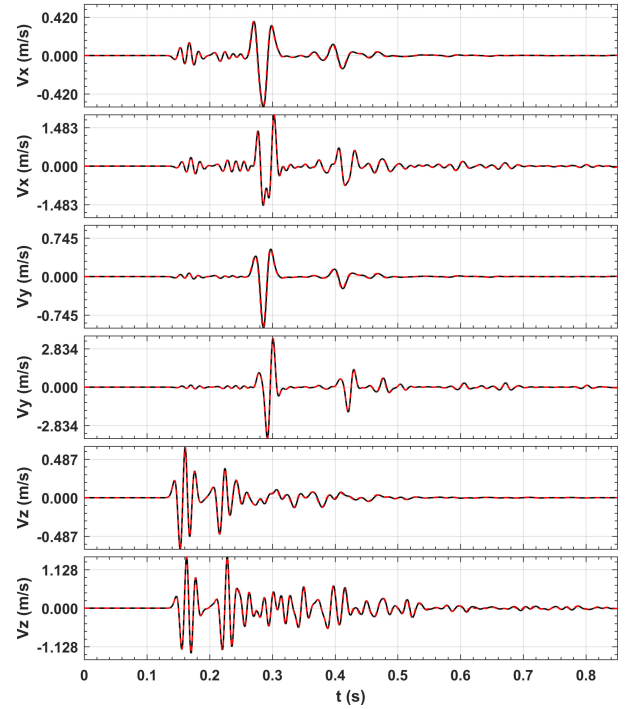
Fig. 4. Multilayer model with the hp-adaptivity technique, the top surface is with free boundary condition; whereas all other boundaries are with perfectly matched layers [29].

TABLE II
POROELASTIC PARAMETERS FOR THE MULTILAYER MODEL

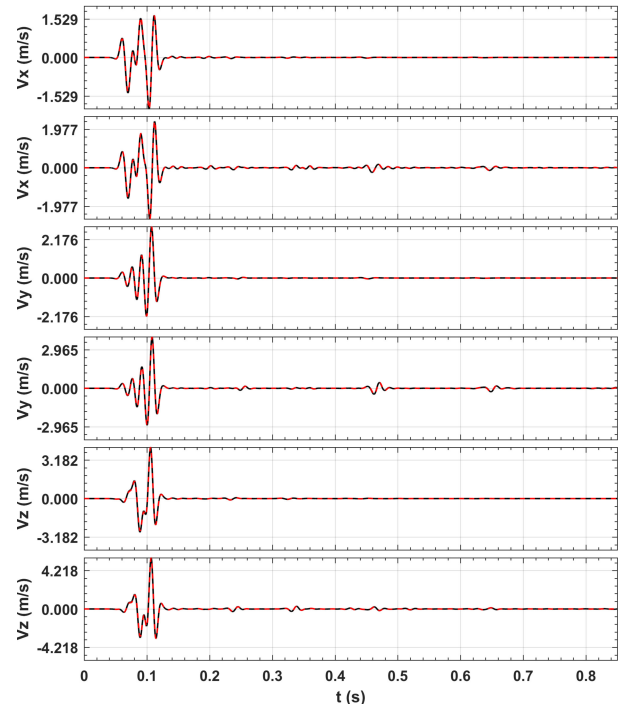
	Layer 1	Layer 2	Layer 3	Layer 4	Layer 5
Mineral [32, T A.4.1]	Kaolinite	Gulf clays	Biotite	Dravite	Muscovite
Upper Interface (m)	0	-100	-300	-500	-550
$Q_{\bar{K}}$	25	35	45	∞	70
Q_S	20	20	25	∞	50
Q_{K_f}	35	35	15	∞	80
Q_{K_s}	20	35	35	∞	50
\bar{K} (GPa)	1.5	21	41.1	102.1	42.9
μ^m (GPa)	1.4	7	12.4	78.7	22.2
K_f (GPa)	2	2.25	1.7	2.295	4.25
K_s (GPa)	8	30	45	106	50
ρ_s (kg/m ³)	1580	2600	3050	3050	2790
ρ_f (kg/m ³)	950	1000	850	1020	1200
T	3	1	2	1	1
ν/κ (Pa·s/D)	1e6	0.333e4	0.5e6	1e3	1e5
ϕ	0.4	0.2	0.3	0.2	0.1
Order	11	9	11	10	10
C_{Ps} (m/s)	587	1470	1014	1512	1848
C_{Pf} (m/s)	2131	3827	5048	9219	5376
C_S (m/s)	1080	1834	2341	5679	2973

in Table II. With the flexibility of our domain decomposition technique: adaptive distributions of the approximation orders, mesh sizes, and anelastic variable allocation are achieved, helping strike the balance between accuracy versus efficiency.

A point source is located at (300, 200, -600) m in the fifth layer. It is added in (1a) as $(F_x^1, F_y^1, F_z^1) = (1, 2, 3) \times S(t)$, where $S(t)$ is the Ricker wavelet as the source time function with the peak frequency $f_c = 40$ Hz. The reference solutions are obtained from an FDTD algorithm, based on the GZB model [33], [34], as implemented by the FDTD solver in [35]. Fig. 5 displays the waveform comparisons for the viscous poroelastic and purely poroelastic media. We can find that the Q factors have a tangible distortion on the waveforms, by attenuating the high-frequency components more than the low-frequency, especially for the reflected wavelets, and slightly left shifting the waveforms. The dissipation and dispersion are more obvious in Fig. 5(a) than Fig. 5(b), due to the longer distance propagation. Furthermore, the memory and time consumptions from the purely poroelastic modeling and viscous poroelastic modeling with three relaxation mechanisms are compared in Table III, respectively, showing only 31% and 25% extra costs. This fact elucidates the superiority of our new ODE-based algorithm.



(a)



(b)

Fig. 5. Waveform comparisons of the solid particle velocity for the receivers at (a) (100, 100, -70) and (b) (100, 100, -560) in the first and fifth layers, respectively. Note that the black solid lines come from the FDTD algorithm, while the red dashed from the DG; the odd rows correspond to viscous poroelastic model, while the even for the purely poroelastic.

C. Nonconformal Mesh Technique Applied to Topography Modeling

Next, we apply our algorithm to the modeling of realistic complex topography by fully utilizing the flexibility of the nonconformal mesh technique. Fig. 6 shows the configuration,

TABLE III

MEMORY AND TIME COMPARISONS BETWEEN PURELY POROELASTIC AND VISCOUS POROELASTIC MODELING

	Memory (GB)	Time (m)
Purely poroelastic	9.5418	134.5495
Viscous poroelastic (3 Mechanisms)	12.4909	168.7422

TABLE IV

POROELASTIC PARAMETERS FOR A TOPOGRAPHY MODELING

	Layer 1	Layer 2	Layer 3
Mineral [32, T A.4.1]	Kerogen	Sylvite	Calcite
$Q_{\bar{K}}$	15	35	20
Q_S	20	40	25
Q_{K_f}	15	22	100
Q_{K_s}	10	22	100
K (GPa)	2.9	17.4	68.3
μ^m (GPa)	2.7	9.4	28.4
K_f (GPa)	1.75	2.25	3.0
K_s (GPa)	3.0	20	70
ρ_s (kg/m ³)	1300	1990	2710
ρ_f (kg/m ³)	800	1000	1200
T	5	2	1
ν/κ (Pa·s/D)	1e5	2e4	1e3
ϕ	0.1	0.15	0.1
Order	10	11	11
C_{P_s} (m/s)	846	1068	1606
C_{P_f} (m/s)	2296	4120	6604
C_S (m/s)	1479	2307	3412

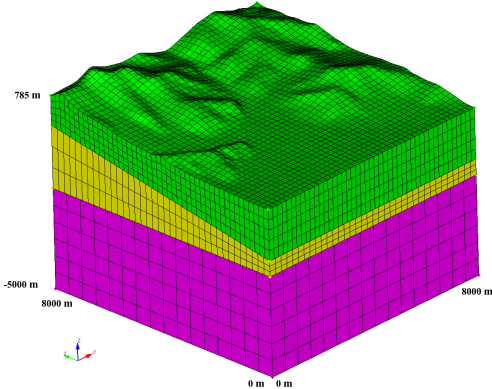


Fig. 6. Realistic topography modeling with the hp-adaptivity technique. The top surface is with free boundary condition; whereas all other boundaries are with perfectly matched layers. A second-order mesh mapping technique is utilized to capture the variance of the ground. The two heterogeneous interfaces are on a plane, determined by three vertices $\{(8000, 0, -1523.14), (0, 0, -1523.14), (0, 8000, -112.52)\}$ m, and another plane $Z = -2000$ m.

where the Tibetan topography is used (28.6° N, 88.3° E to 28.5° N, 88.4° E). The satellite data is downloaded from <http://srtm.csi.cgiar.org/SELECTION/inputCoord.asp> (last accessed November, 2018). A z-polarized source with a Ricker wavelet of 5-Hz central frequency, added in (1a), is located at (300, 300, -2100) m in the bottom layer. Table IV provides the material properties from the top layers to the bottom. The whole computational domain is about $175\lambda_{\min} \times 175\lambda_{\min} \times 136\lambda_{\min}$ in X, Y , and Z directions, where λ_{\min} is the minimum wavelength corresponding to $3.5f_c$. To improve the simulation efficiency but without

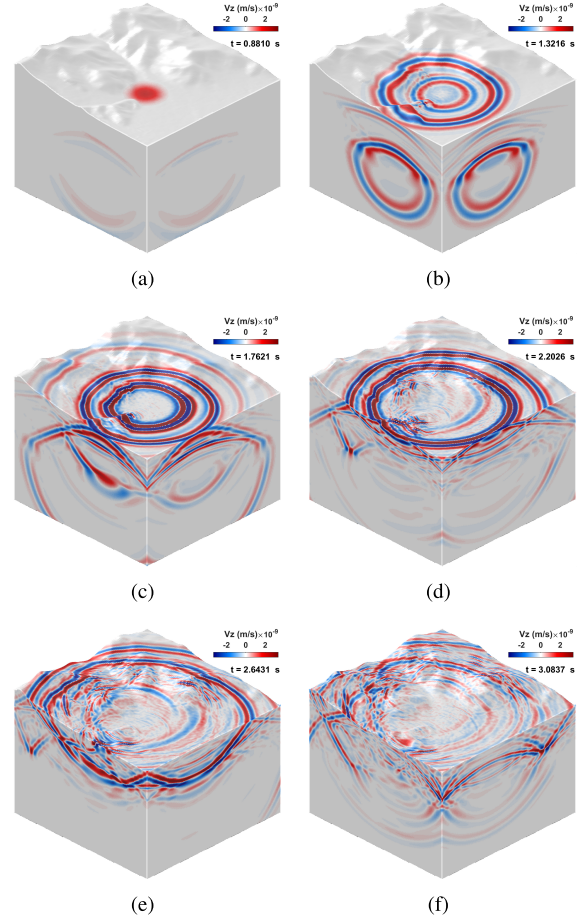


Fig. 7. Snapshots of v_z distribution on the ground and cut surfaces recorded with equidistant time intervals.

scarifying accuracy, we apply the domain decomposition technique by adaptively distributing nonconformal meshes and nonuniform basis function orders. Fig. 7 shows the snapshots for the vertical component of the solid particle velocity. The transmitted fast P waves hit the ground in Fig. 7(a), then the S waves arrive and spread in Fig. 7(b), followed by a slow P wave shown in Fig. 7(c), where the surface waves become conspicuous between the interfaces [36]. As time moves on, the reflected waves, from the interface between the first and second layers, propagate back to the ground. Conspicuous scattering is observed from the small peaks on the ground in Fig. 7(d). The fields are very complicated due to the interactions between waves and the topography in Fig. 7(e) and (f).

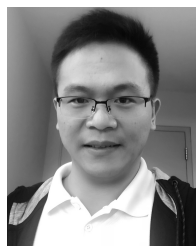
VII. CONCLUSION

A complete-Q model, comprised of four quality factors, is proposed to depict the dissipation and dispersion of poro-viscoelastic media in realistic subsurface sensing. Based on the velocity-strain variables, the Riemann problem of the new hyperbolic system is exactly solved for an adaptive nonconformal-mesh discontinuous Galerkin method. Furthermore, the auxiliary equations are just ordinary differential equations, thus leading to an efficient evaluation of the anelastic functions. The verification and validation with an analytical

solution and an independent code demonstrate the high flexibility, accuracy, and efficiency of the proposed method.

REFERENCES

- [1] Y.-F. Sun, "Seismic signatures of rock pore structure," *Appl. Geophys.*, vol. 1, no. 1, pp. 42–49, Jul. 2004.
- [2] H. Hu, W. Guan, and J. M. Harris, "Theoretical simulation of electroacoustic borehole logging in a fluid-saturated porous formation," *J. Acoust. Soc. Amer.*, vol. 122, no. 1, pp. 135–145, 2007.
- [3] Y. Zhang, J. Gao, and J. Peng, "Variable-order finite difference scheme for numerical simulation in 3-D poroelastic media," *IEEE Trans. Geosci. Remote Sens.*, vol. 56, no. 5, pp. 2991–3001, May 2018.
- [4] J. M. Carcione, *Wave Fields in Real Media: Wave Propagation in Anisotropic, Anelastic, and Porous Media* (Handbook of Geophysical Exploration. Seismic Exploration), vol. 31. New York, NY, USA: Pergamon, 2001, pp. 950–1401.
- [5] J. M. Carcione, "Theory and modeling of constant- Q P- and S-waves using fractional time derivatives," *Geophysics*, vol. 74, no. 1, pp. T1–T11, 2008.
- [6] J.-G. Liu, Z. Ma, and Z. Zhou, "Explicit and implicit TVD schemes for conservation laws with Caputo derivatives," *J. Sci. Comput.*, vol. 72, no. 1, pp. 291–313, 2016.
- [7] L. Li and J.-G. Liu, "A note on deconvolution with completely monotone sequences and discrete fractional calculus," *Quart. Appl. Math.*, vol. 76, no. 1, pp. 189–198, 2018.
- [8] P. Moczo, J. Kristek, and M. Gális, *The Finite-Difference Modelling of Earthquake Motions: Waves and Ruptures*. Cambridge, U.K.: Cambridge Univ. Press, 2014.
- [9] J. Chen and J. Wang, "Three-dimensional dispersive hybrid implicit-explicit finite-difference time-domain method for simulations of graphene," *Comput. Phys. Commun.*, vol. 207, pp. 211–216, Oct. 2016.
- [10] M. Käser, M. Dumbser, J. De La Puente, and H. Igel, "An arbitrary high-order discontinuous Galerkin method for elastic waves on unstructured meshes—III. Viscoelastic attenuation," *Geophys. J. Int.*, vol. 168, no. 1, pp. 224–242, Jan. 2007.
- [11] Y. Zhang, I. Nault, S. Mitran, E. S. Iversen, and P. Zhong, "Effects of stone size on the comminution process and efficiency in shock wave lithotripsy," *Ultrasound Med. Biol.*, vol. 42, no. 11, pp. 2662–2675, Nov. 2016.
- [12] Y. Zhang, Y. Zhuang, and L. Zhang, "A new high-order finite volume method for 3D elastic wave simulation on unstructured meshes," *J. Comput. Phys.*, vol. 340, pp. 534–555, Jul. 2017.
- [13] J. de la Puente, M. Dumbser, M. Käser, and H. Igel, "Discontinuous Galerkin methods for wave propagation in poroelastic media," *Geophysics*, vol. 73, no. 5, pp. T77–T97, 2008.
- [14] Q. Zhan *et al.*, "Efficient ordinary differential equation-based discontinuous Galerkin method for viscoelastic wave modeling," *IEEE Trans. Geosci. Remote Sens.*, vol. 55, no. 10, pp. 5577–5584, Oct. 2017.
- [15] E. Kjartansson, "Constant Q -wave propagation and attenuation," *J. Geophys. Res.*, vol. 84, no. B9, pp. 4737–4748, Aug. 1979.
- [16] P. Zheng, S.-X. Zhao, and D. Ding, "Dynamic Green's functions for a poroelastic half-space," *Acta Mech.*, vol. 224, no. 1, pp. 17–39, 2013.
- [17] H. Emmerich and M. Korn, "Incorporation of attenuation into time-domain computations of seismic wave fields," *Geophysics*, vol. 52, no. 9, pp. 1252–1264, 1987.
- [18] Q. Zhan, Q. Ren, Q. Sun, H. Chen, and Q. H. Liu, "Isotropic Riemann solver for a nonconformal discontinuous Galerkin pseudospectral time-domain algorithm," *IEEE Trans. Geosci. Remote Sens.*, vol. 55, no. 3, pp. 1254–1261, Mar. 2017.
- [19] Q. Zhan, Q. Sun, Q. Ren, Y. Fang, H. Wang, and Q. H. Liu, "A discontinuous Galerkin method for simulating the effects of arbitrary discrete fractures on elastic wave propagation," *Geophys. J. Int.*, vol. 210, no. 2, pp. 1219–1230, 2017.
- [20] J. Chen, "An efficient discontinuous Galerkin finite element method with nested domain decomposition for simulations of microresistivity imaging," *J. Appl. Geophys.*, vol. 114, pp. 116–122, Mar. 2015.
- [21] J. Xu, J. Bielak, O. Ghattas, and J. Wang, "Three-dimensional nonlinear seismic ground motion modeling in basins," *Phys. Earth Planetary Interiors*, vol. 137, nos. 1–4, pp. 81–95, May 2003.
- [22] M. Li, V. Druskin, A. Abubakar, and T. M. Habashy, "A 2.5D finite-difference algorithm for elastic wave modeling using near-optimal quadratures," *Geophysics*, vol. 81, no. 4, pp. T155–T162, 2016.
- [23] C. Meng and H. Wang, "A finite element and finite difference mixed approach for modeling fault rupture and ground motion," *Comput. Geosci.*, vol. 113, pp. 54–69, Jan. 2018.
- [24] J. Chen and Q. H. Liu, "Discontinuous Galerkin time-domain methods for multiscale electromagnetic simulations: A review," *Proc. IEEE*, vol. 101, no. 2, pp. 242–254, Feb. 2013.
- [25] Q. Zhan, Q. Ren, M. Zhuang, Q. Sun, and Q. H. Liu, "An exact Riemann solver for wave propagation in arbitrary anisotropic elastic media with fluid coupling," *Comput. Methods Appl. Mech. Eng.*, vol. 329, pp. 24–39, Feb. 2018.
- [26] Q. Zhan *et al.*, "A new upwind flux for a jump boundary condition applied to 3D viscous fracture modeling," *Comput. Methods Appl. Mech. Eng.*, vol. 331, pp. 456–473, Apr. 2018.
- [27] E. F. Toro, *Riemann Solvers and Numerical Methods for Fluid Dynamics: A Practical Introduction*. New York, NY, USA: Springer, 2009.
- [28] Q. Zhan, M. Zhuang, and Q. H. Liu, "A compact upwind flux with more physical insight for wave propagation in 3-D poroelastic media," *IEEE Trans. Geosci. Remote Sens.*, vol. 56, no. 10, pp. 5794–5801, Oct. 2018.
- [29] Q. Zhan, Q. Ren, Q. Sun, and Q. H. Liu, *Discontinuous Galerkin Pseudospectral Time Domain Algorithm (DG-PSTD) With Auxiliary Ordinary Differential Equations Perfectly Matched Layer (AODE-PML) for 3D Seismic Modelling*. New Orleans, LA, USA: Society of Exploration Geophysicists, 2015, pp. 3633–3638.
- [30] H. Wang, G. Tao, and K. Zhang, "Wavefield simulation and analysis with the finite-element method for acoustic logging while drilling in horizontal and deviated wells," *Geophysics*, vol. 78, no. 6, pp. D525–D543, 2013.
- [31] Q. H. Liu, "The PSTD algorithm: A time-domain method requiring only two cells per wavelength," *Microw. Opt. Technol. Lett.*, vol. 15, no. 3, pp. 158–165, Jun. 1997.
- [32] G. Mavko, T. Mukerji, and J. Dvorkin, *The Rock Physics Handbook: Tools for Seismic Analysis of Porous Media*. Cambridge, U.K.: Cambridge Univ. Press, 2009.
- [33] M. Zhuang, Q. Zhan, J. Zhou, N. Liu, and Q. H. Liu, "Incorporating full attenuation mechanisms of poroelastic media for realistic subsurface sensing," *IEEE Trans. Geosci. Remote Sens.*, to be published. [Online]. Available: <https://ieeexplore.ieee.org/document/8492340>, doi: 10.1109/TGRS.2018.2871375.
- [34] Y. Q. Zeng and Q. H. Liu, "A staggered-grid finite-difference method with perfectly matched layers for poroelastic wave equations," *J. Acoust. Soc. Amer.*, vol. 109, no. 6, pp. 2571–2580, 2001.
- [35] Wave Computation Technologies, Inc. (2018). *Wavenology EL Solvers*. [Online]. Available: <http://www.wavenology.com>
- [36] H. Wang, M. Fehler, and D. Miller, "Reliability of velocity measurements made by monopole acoustic logging-while-drilling tools in fast formations," *Geophysics*, vol. 82, no. 4, pp. D225–D233, Jul./Aug. 2017.



Qiwei Zhan (S'16) received the B.S. degree in Geophysics from the University of Science and Technology of China, Hefei, China, in 2013, and the M.S. degree in civil and environmental engineering from Duke University, Durham, NC, USA, in 2016, where he is currently pursuing the Ph.D. degree with the Department of Electrical and Computer Engineering.

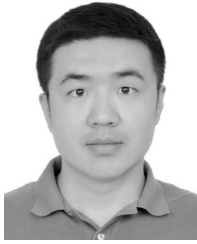
His research interests include computational acoustics, computational electromagnetics, anisotropic homogenization theory, high-speed cables, inverse problems, and biomedical imaging.

Mr. Zhan was a recipient of the 2017–2019 John T. Chambers Scholar Award at Duke University.



Mingwei Zhuang received the Ph.D. degree in radio physics from Xiamen University, Xiamen, China, in 2018.

From 2016 to 2017, he was a Visiting Student with the Department of Electrical and Computer Engineering, Duke University, Durham, NC, USA. His research interests include numerical methods in acoustic/viscoelastic/poroelastic waves and imaging.



Zhennan Zhou received the M.A. and Ph.D. degrees in applied math from the University of Wisconsin-Madison, Madison, WI, USA, in 2011 and 2014, respectively.

He was a William W. Elliott Assistant Research Professor at the Mathematics Department, Duke University, Durham, NC, USA, from 2014 to 2017. He is currently a Tenure-Track Assistant Professor at the Beijing International Center for Mathematical Research, Peking University, Beijing, China.

His research interests include semiclassical and multiscale methods in quantum dynamics, band transition for Bloch electrons, kinetic theory, Born–Oppenheimer approximation and numerical methods for conservation laws, and clustering algorithms.



Jian-Guo Liu received the B.S. and M.S. degrees from Fudan University, Shanghai, China, in 1982 and 1985, respectively, and Ph.D. degree from the University of California at Los Angeles, Los Angeles, CA, USA, in 1990. He is currently a Professor of Department of Physics and Department of Mathematics, Duke University, Durham, NC, USA. His research interests include partial differential equations, kinetic theory, computational fluid dynamics, nonlinear dynamics, fluid dynamics, complex fluids, emergent behavior and self-organization, etc.

Dr. Liu is a Fellow of American Mathematical Society. He is currently a Co-Editor of the *Journal of Hyperbolic Differential Equations*.



Qing Huo Liu (S'88–M'89–SM'94–F'05) received the B.S. and M.S. degrees in physics from Xiamen University, China, and the Ph.D. degree in electrical engineering from the University of Illinois at Urbana–Champaign, Champaign, IL, USA.

He was a Research Scientist and a Program Leader of Schlumberger-Doll Research, Ridgefield, CT, USA, from 1990 to 1995. From 1996 to 1999, he was an Associate Professor with New Mexico State University, Las Cruces, NM, USA. He was with the Electromagnetics Laboratory, University of Illinois at Urbana–Champaign, as a Research Assistant, from 1986 to 1988, and as a Post-Doctoral Research Associate, from 1989 to 1990. He has published over 500 papers in refereed journals and numerous papers in conference proceedings. Since 1999, he has been with Duke University, Durham, NC, USA, where he is currently a Professor of electrical and computer engineering. His research interests include computational electromagnetics and acoustics, and inverse problems and their applications in nanophotonics, geophysics, biomedical imaging, and electronic packaging.

Dr. Liu is a fellow of the IEEE, the Acoustical Society of America, The Electromagnetics Academy, and The Optical Society of America. He has served as an IEEE Antennas and Propagation Society Distinguished Lecturer. He has received the 2017 Technical Achievement Award and the 2018 Computational Electromagnetics Award from the Applied Computational Electromagnetics Society, and the 2018 Harrington-Mittra Award in Computational Electromagnetics from the IEEE Antennas and Propagation Society. He has received the 1996 Presidential Early Career Award for Scientists and Engineers from the White House, the 1996 Early Career Research Award from the Environmental Protection Agency, and the 1997 CAREER Award from the National Science Foundation. He currently serves as the founding Editor-in-Chief of the new IEEE JOURNAL ON MULTISCALE AND MULTIPHYSICS COMPUTATIONAL TECHNIQUES.